Quantitative imaging of freezing at the millimeter scale using neutron radiography

A.J. Gilbert, M.R. Deinert *

Department of Mechanical Engineering, The University of Texas at Austin, United States

A B S T R A C T

Freezing of fluids in capillary structures affects systems that range from soils to the polymer membranes that are used in fuel cells. Neutron radiography can be used to image phase change within otherwise opaque structures and previous studies have shown the capability of quantitative imaging of freezing at ~ 3 mm scale. In this study, a 1.6 mm diameter water column within an aluminum rod was imaged using neutron radiography and fluid density information was extracted. A ray-tracing flux model was developed in order to correct for the effects of beam divergence on the acquired images. The model produced image intensity maps that fit experimental data with R^2 values of 0.98. Density measurements for water and ice within the capillary were found to be 1.00 ± 0.03 and 0.93 ± 0.03 g/cm^3, respectively, which are within 1% of published density values for both phases.

© 2011 Elsevier B.V. All rights reserved.

1. Introduction

Freezing and melting phenomena within capillary structures are important to understanding a wide variety of processes including the structuring of soils, environmental fluid transport, catalysis, and fluid transport within functioning fuel cells. Unfortunately, the physical structures of the systems in which these processes take place create significant challenges if quantitative imaging is used to study them. If the fluids in question are hydrogenous, then neutron radiography can have significant advantages over standard imaging techniques that use x-rays or magnetic resonance imaging. The neutron cross-section for hydrogen is large compared to many heavier elements, consequently providing a greater contrast in images than that when using complementary imaging techniques. Previous studies have used neutron radiography for quantitative imaging of rapidly translating wetting fronts and moisture profiles in porous materials (e.g. [1–4]). The technique has also been used to visualize and measure water production and flow within a proton exchange membrane fuel cell (e.g. [5–10]). A method for quantifying water phase change via neutron radiography has also been explored (e.g. [11]). The work in [11] used neutron computed tomography and neutron radiography to quantify the density of a 2.95 mm diameter column of water in solid and liquid phase to within 2% of known values.

The current contribution extends the development of quantitative neutron radiography for measurements of water phase change at the millimeter scale. A ray-tracing model for the image plane neutron flux has been developed to correct for the effects of beam divergence. The system response was determined using a calibration standard. The system was found to be capable of density measurements to within 1% of known values at 1.6 mm scale.

2. Materials and methods

A TRIGA Mark II Research Reactor located at the University of Texas at Austin was used as the neutron source for this work. The reactor is capable of 1.1 MW steady state power. The thermal neutron imaging facility is located on a tangential neutron beam port in which the thermal neutron flux at 500 kW steady state operation has been previously determined via gold foil activation to be 1.21×10^6 neutrons/cm^2-s with a cadmium ratio of 2.6 and beam diameter of 22.5 cm [12], Fig. 1a. The *L/D* ratio, determined from collimator geometry, is 121. To reduce exposure time, reactor power is held at 950 kW, the maximum allowable power for experiments in order to stay below regulatory limits. The beam port flux increases proportionally with reactor power.

In this work, a $254 \times 254 \times 0.3$ mm^3 Applied Scintillation Technologies LiF/ZnS scintillator screen was used. Visible light from the scintillator screen is reflected into a CCD camera using a front surface mirror, Fig. 1b. The CCD camera was an Andor iXon+ 885 EMCCD with a 1004×1002 active pixel area on the chip, 8×8 μm pixel size, a dynamic range of 14 bits, and is cooled

* Corresponding author.
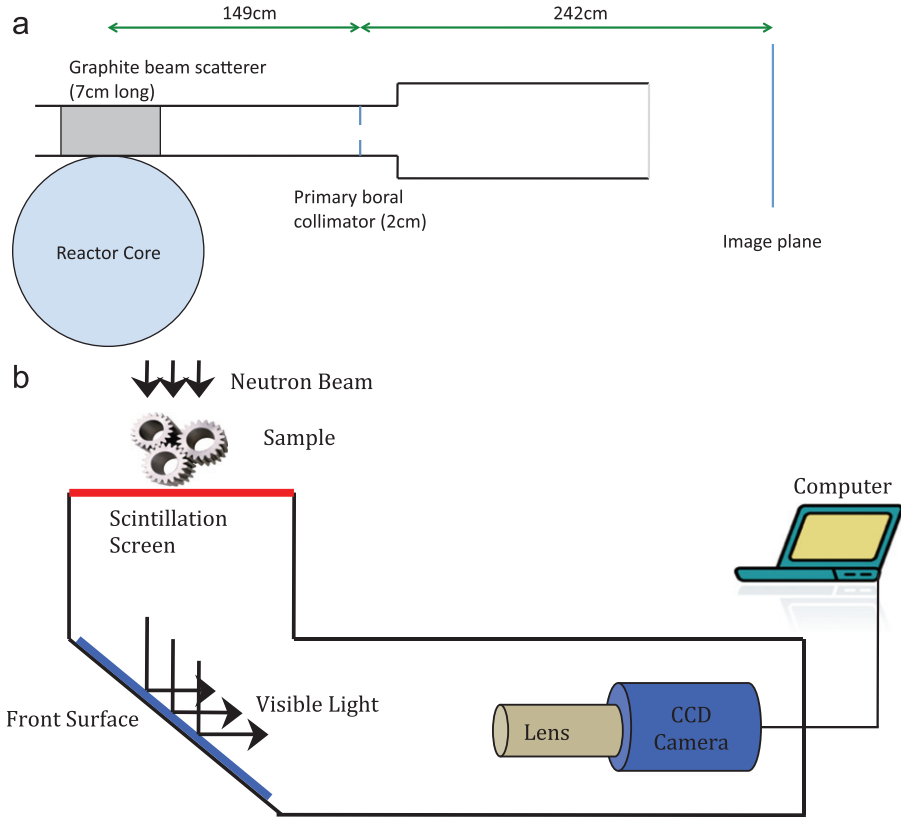 *E-mail address:* mdeinert@mail.utexas.edu (M.R. Deinert).

Fig. 1. Experimental schematic. (a) Beam port tangential collimator. Shown are the primary boral collimator and the distances from the image plane to the neutron source, here a graphite beam scatterer placed next to the reactor core. (Not to scale). (b) Schematic of the beam port neutron radiography image acquisition setup.

to $-70\ ^\circ$C. Camera field-of-view was $64 \times 64\ mm^2$ and the spatial resolution, determined from the projection of the detector onto an individual pixel, was 0.064 mm. Digital images were acquired using the iXon Solis software and post-processing was done using NIH ImageJ and Matlab. Exposure time for all acquired images was 180 s. The camera was protected from direct and secondary gamma radiation using lead, polyethylene, and a 3.2 mm sheet of flexible boron shielding.

The sample piece developed for this work was a 9.53 mm OD 6061 aluminum rod cut to 70 mm length with a 0.16 cm diameter blind hole drilled into the middle. This geometry, instead of a plate geometry, was used for ease of machining and good precision on actual thicknesses expected. The cavity was filled with degassed water and the sample piece was frozen using dry ice. To prevent condensation build-up on the aluminum surface during the freezing process, the sample was placed in a thin-walled Teflon® FEP bag, which was flushed with dry nitrogen. It was observed that condensation did not build up on the outside of the Teflon® bag during experiments.

3. Temperature effects

The density of water and ice will vary significantly with temperature. To determine the temperatures the sample will reach during the experiment in the beam port, a separate study was set up using a Mikron TH7515 IR camera for thermal imaging while the sample was cooled and warmed. The aluminum sample filled with water was clamped in place with dry ice placed around it within a plastic bag flushed with dry oxygen, similar to the experimental setup in the beam port. Dry oxygen gas was used for this experiment, instead of the dry nitrogen used in the radiography setup, due to its availability when this experiment was conducted. With dry ice

in place the sample reached a temperature equilibrium at $-20 \pm 1\ ^\circ$C. Then, the dry ice was removed and the sample was allowed to thaw for 45 min, when it reached $10 \pm 1\ ^\circ$C. From this temperature data, an expected initial and final water density of 0.92 and $1.00\ g/cm^3$ were determined, respectively [13].

4. Data acquisition and processing

A plane beam of neutron flux, $\phi(x)$, will be attenuated by a material according to:

$$\phi(x)/\phi_0 = B\ exp\left[-\int \sum_t dz\right], \qquad (1)$$

where ϕ_0 is the initial neutron flux, Σ_t is the cross-section of the material, and z is the thickness of the material through which the beam is traveling. Here B represents the "buildup" factor, which accounts for neutrons that will scatter within the object or in the surrounding experimental setup in such a way as to be incident on the image plane. The contributions to neutron flux at the image plane, ϕ, are unattenuated neutrons, ϕ_{un}, scattered neutrons from the sample, $\phi_{s,sample}$, and scattered neutrons from the surrounding materials in the beam port, $\phi_{s,surroundings}$, as shown here:

$$\phi = \phi_{un} + \phi_{s,sample} + \phi_{s,surroundings} \qquad (2)$$

Scattering from the sample was limited in this work by the small sample size and dispersion due to a sample to image plane separation of 5 cm, (e.g. [15]). The constant flux of neutrons scattered from the surroundings is accounted for in the system calibration, discussed below.

A dark current image was subtracted from each sample image. The dark current image was obtained by covering the camera

lens, cooling the camera to $-70\,^{\circ}C$ and obtaining an image with the beam port closed and reactor at 950 kW. In order to compare one data set to another, each image was normalized to account for fluctuations in reactor power. Reactor power averaged over 3 min intervals was observed to vary by as much as 2.2%. To account for these fluctuations, all images were normalized to an average background pixel value of a reference image taken from each data set. Each image was then divided by an image of the empty sample container, which divides out the effects of the beam profile and aluminum on the images, leaving only the effect of the water, Fig. 2.

Images were obtained using a 180 s exposure time with reactor power at 950 kW. To obtain a single data vector for each image and reduce noise, horizontal scan lines of 81 pixels wide were extracted across the water column, centered at the full thickness of the column. 250 of these scan lines were averaged to get the single data vector for the image. The final data vectors presented in the results section are the average of 8 of these data vectors from separate experiments.

As in [14,15], we found that the response of the imaging system to changes in neutron flux is well described using:

$$I/I_0 = a\Delta\phi/\phi_0 + 1 \qquad (3)$$

here I and I_0 are the attenuated and unattenuated image intensities resulting from an initial flux, ϕ_0, and a is a constant to take into account the system response, which includes the scattered flux contribution given as the "buildup" factor in Eq. (1). The difference in neutron flux due to attenuation, $\Delta\phi$, is given by

$$\Delta\phi = [exp(-\textstyle\sum_t z) - 1]\phi_0. \qquad (4)$$

Combining Eqs. (3) and (4) gives:

$$I/I_0 = a\,exp(-\textstyle\sum_t z) + (1-a), \qquad (5)$$

which can be used to relate a value of image intensity to a material's macroscopic cross-section.

To find the constant a, the cross-section of a polystyrene step standard was found experimentally in the beam port to be $2.63 \pm 0.02\,cm^{-1}$ by measuring neutron transmission with a BF_3 detector. Since the BF_3 detector literally counts neutrons without effect from other factors, such as those in the imaging system, it was used to determine the actual cross-section in the beam port. Next, the step standard was placed in the radiography setup and imaged in the same manner as the water column. Polystyrene was selected as the step standard material due to its hydrogen content similar to that of water. Shown in Fig. 3, the radiography system response, I/I_0, is plotted with respect to the expected attenuation showing how the image intensity changes according to attenuation. From this, a system response value of 0.819 ± 0.003 was obtained, which can be used to relate image intensity to the cross-section via Eq. (5). It was noted that the detection isotope for this experiment, ^{10}B, was different from that of the scintillation screen, ^6Li. However, since the cross-section energy dependence for these isotopes are nearly identical in the thermal and epithermal energies, this difference will not affect the final results.

5. Measuring density

Assuming a constant microscopic cross-section of water in the temperature range for our experiment, the density can be measured directly by comparing the calculated macroscopic cross-section to published values of water where [16]:

$$\Sigma_{t,water} = 3.47\,cm^{-1} \qquad (6)$$

The ice cross-section is expected to decrease by 8% from the water cross-section, proportional to the density change between water and ice, as explained in the temperature effects section above. This cross-section is valid for a thermal neutron spectrum, assumed for this work. As shown in Fig. 1a, the beam port looks through the collimator into a graphite reflector, which is at the edge of the water surrounding the reactor core. This results in a
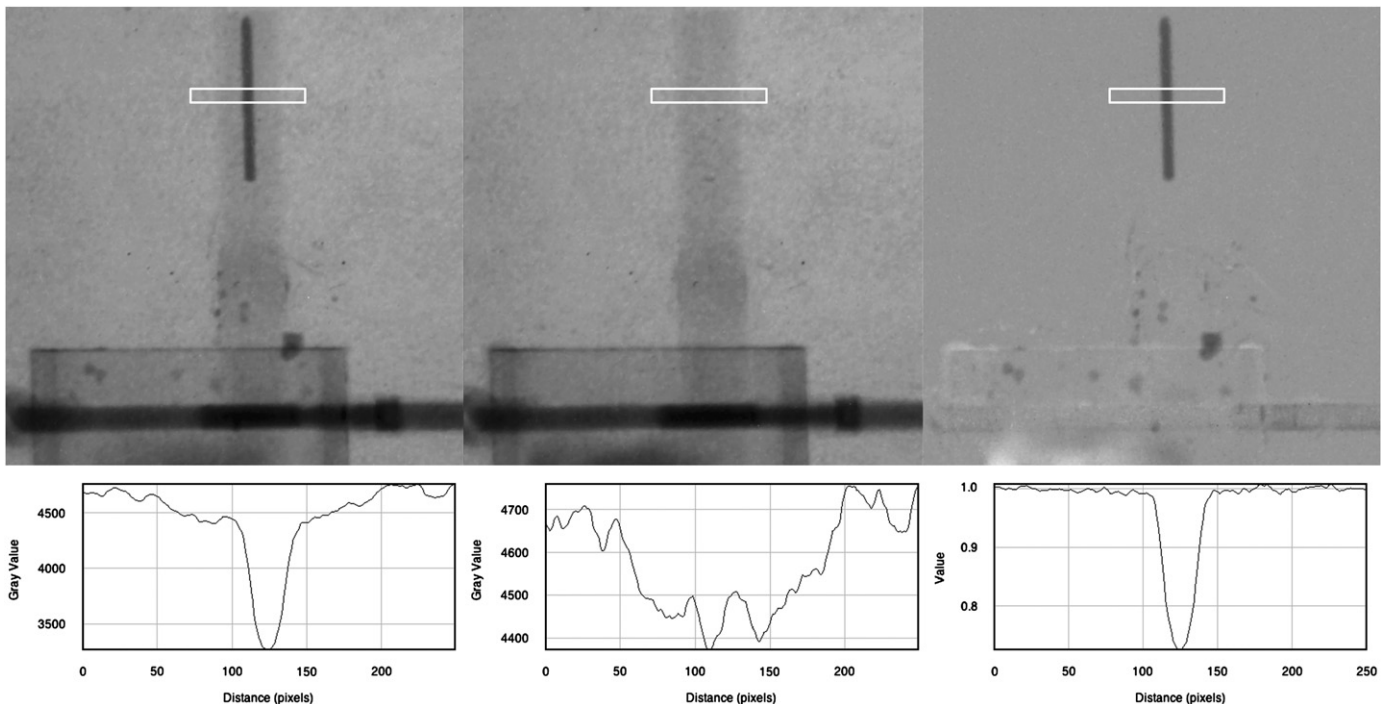

Fig. 2. Image normalization. From left to right, image normalization by dividing sample image by blank sample image. Images are, from left to right, original sample, blank Al sample, and divided image. The dark image has been subtracted from the original and blank Al images. Plots of intensity vs. average pixel value for a region of interest, within the white rectangle, for each image are shown under each image to show how this normalization removes both beam asymmetry and aluminum attenuation from the image. The Teflon bag flushed with dry nitrogen used to reduce condensation on the sample is practically invisible in the images.
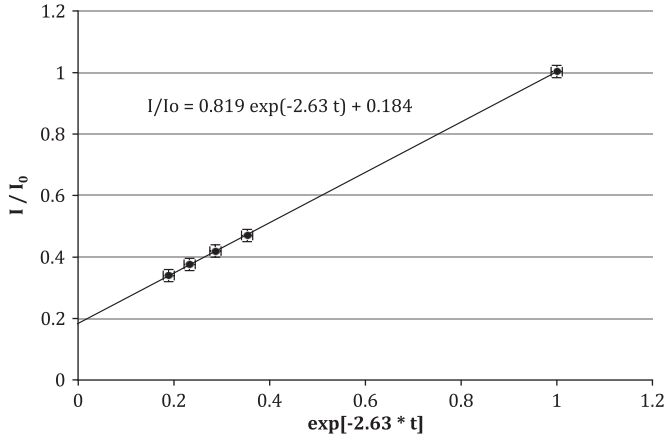
I/Io = 0.819 exp(-2.63 t) + 0.184

Fig. 3. System calibration. To find the relationship of intensity output from the CCD camera to neutron attenuation from a target, I/I_0 values from experimental radiographs are plotted with respect to theoretical flux attenuation expectations for a polystyrene step standard, the cross-section of which was determined experimentally in the beam port. The slope of this fit corresponds to the correction factor, a. The plot also shows, from the y-intercept, that the system has a background contribution of about %18 from the contribution of scattered neutrons and the imaging system.

Fig. 4. Ray tracing geometry. A single ray of angular flux incident on the image plane (not to scale). The flux model calculates the flux at the image plane by taking into account all possible rays of flux from the collimator to the image plane, with or without impinging on the sample.

Fig. 5. Flux model results at the image plane with various source sizes. This shows that though the shape of the flux profile at the edges changes noticeably, the minimum value of I/I_0 changes slightly. This validates the use of Eq. (7) for making density measurements based on the minimum I/I_0 value. However, this result does indicate that beam divergence would need to be accounted for in measurements near the sample edge or for tomographic reconstructions.

thermal spectrum at the beam port. Also, beam chopper experiments at the Cornell TRIGA Mark II reactor have shown a thermal neutron spectrum in a beam port very similar to the port in this work [17]. All previous measurements, as well as those done in this study, indicate that the cross sections that have been measured, or assumed, are well justified.

The experimental total cross-section, $\Sigma_{t,ex}$, can be calculated by rearranging Eq. (5), under the assumption that the neutron beam is perfectly collimated:

$$\Sigma_{t,ex} = \frac{-\ln[(I/I_0 - 1)/a + 1]}{z} \qquad (7)$$

where I/I_0 is the experimental image intensity value at sample thickness, z, with system response factor, a.

To measure density from the cross-section measurements, the ratio of the experimental density measured, ρ_{ex}, to actual water density at room temperature, ρ_{water}, is equal to the ratio of the cross-section measured, $\Sigma_{t,ex}$, to water published cross-section, $\Sigma_{t,water}$ as

$$\rho_{ex}/\rho_{water} = \Sigma_{t,ex}/\Sigma_{t,water} \qquad (8)$$

6. Image plane flux model

Eq. (7) only applies when the neutron beam can be assumed to be perfectly collimated or coming from a point source. In order to test this, we developed a ray-tracing model to calculate the image plane neutron flux based on the geometry shown in Fig. 4. This model accounts for the flux at the image plane as a function of the sample and the neutron source as

$$\phi(x) \propto \varphi_0(m,\theta)T(u,\phi) \qquad (9)$$

Here φ_0 [n/cm²-s-ster] is the incoming angular neutron flux from the primary collimator with incoming angle, θ, from each point along the collimator coordinate, m. The function representing the attenuation of rays of flux through the target is T [cm^{-1}] at each point on u. ϕ [n/cm²-s] is the resulting flux at each point, x, along the image plane.

It was determined from the results of the flux model that the geometric divergence of the beam does not have a significant effect on the intensity value around the minimum of the flux,
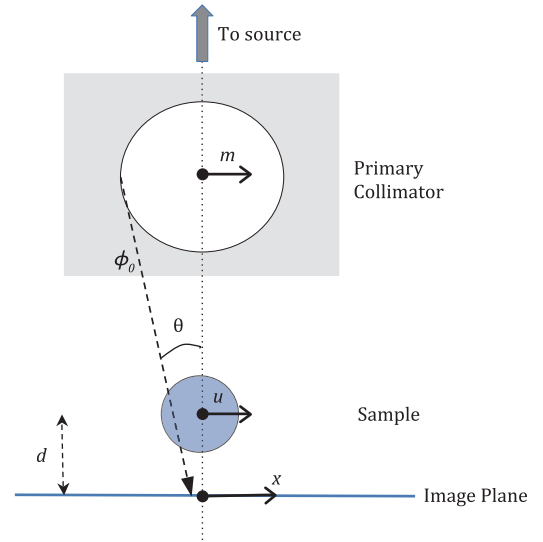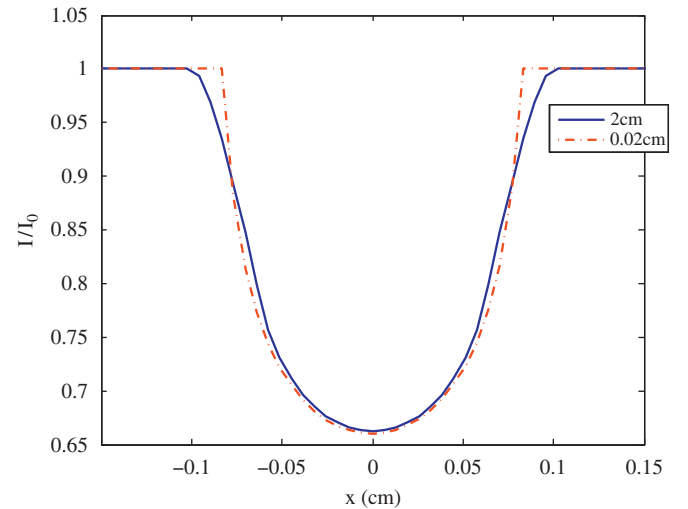
Fig. 5. As the collimator diameter approaches zero, the flux shape approaches that expected from a point source. The difference between minimum values of the flux between the 2 cm and 0.02 cm cases of primary collimator diameter is only 0.4%.

7. Propagation of error

Error on the final density measurement can be calculated by applying error propagation formulae to Eqs. (7) and (8), and assuming that the standard deviations of I/I_0, a, and z are uncorrelated. The standard deviation of a single I/I_0 image is found in a representative background region of the image, with the distribution of the image intensity shown to be Gaussian, e.g. Fig. 6. This standard deviation was reduced significantly by averaging 8 images, which were each averaged over 250 scan

line vectors. Error in a was found using the least squares error analysis on the linear fit to find a. Finally, error in z is the uncertainty associated with the machining process.

From error propagation equations [18], a final standard deviation on the density measurements was found to be ~0.03.

8. Results

Fig. 7 shows the normalized experimental data for water and ice. It is apparent that there is a greater intensity at the full sample thickness of the ice sample compared to water, as would be expected due to the lower density.

Cross sections can be directly calculated by use of Eq. (7), using the minimum experimental I/I_0 for each water phase taken at sample thickness, z, of 0.16 cm. From the minimum I/I_0 values of water and ice data, the calculated Σ_t is 3.48 cm^{-1} and 3.22 cm^{-1}, respectively. The water cross-section agrees well with the

published thermal neutron cross-section for water of 3.47 cm^{-1} [16]. Using Eq. (8), the densities of water and ice at maximum sample thickness are found to be 1.00 ± 0.03 and 0.93 ± 0.03 g/cm^2, respectively, in agreement with expectations of water density to within 1%.

Figs. 8 and 9 show the experimental data after processing and compare the results to those predicted by the flux model. The experimental data shown in these figures is the average of eight separate experimental measurements in which the data obtained has been processed as described above. The flux model plotted for comparison is calculated using water and ice total neutron cross-sections of 3.47 cm^{-1} and 3.19 cm^{-1}, respectively, based on the known thermal total neutron cross-section for water and an 8% difference in water density between the two phases for 10 °C water and -20 °C ice [13]. The predictions fit well with the experimental data with R^2 values of 0.98 for both water and ice. Edge blurring due to scatter and detector particle travel seen in the experimental data are present in all radiography systems. No attempt was made to include these effects in the flux model developed for this study.
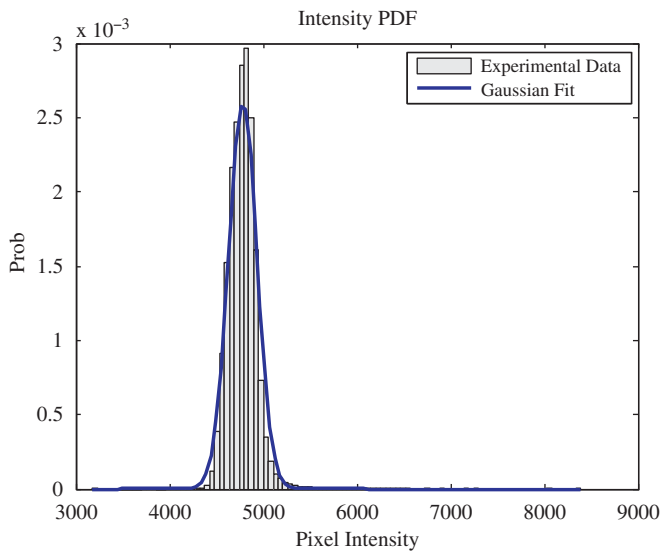

Fig. 6. Statistical distribution of pixel noise. This is an example of the pixel intensity probability distribution function in a background region of an image and is shown to fit well to a Gaussian distribution.
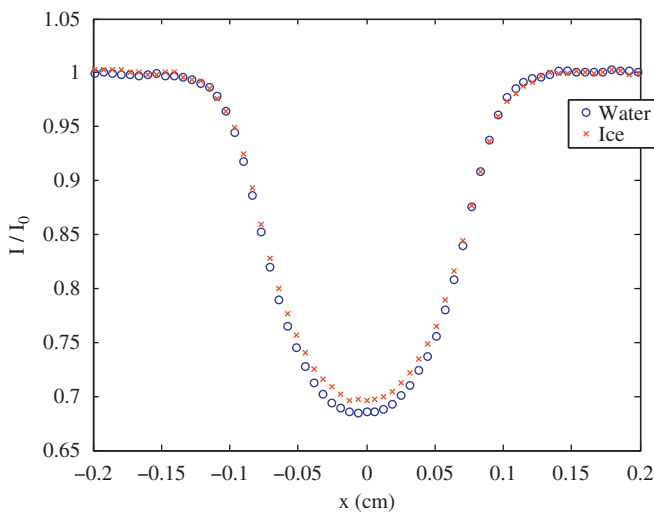

Fig. 8. Measured and predicted neutron attenuation for water. Water column profile from average of eight experiments and theoretical expectation. R^2 here is 0.98.

Fig. 7. Neutron attenuation by water/ice profile comparison. At full sample thickness ($x=0$), the intensity value for ice is noticeably greater than that for water, which is expected due to its lower density. Error bars left off here for clarity of data.
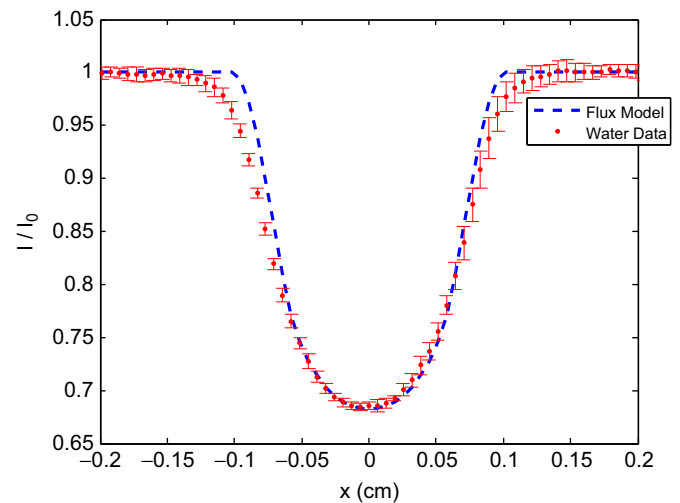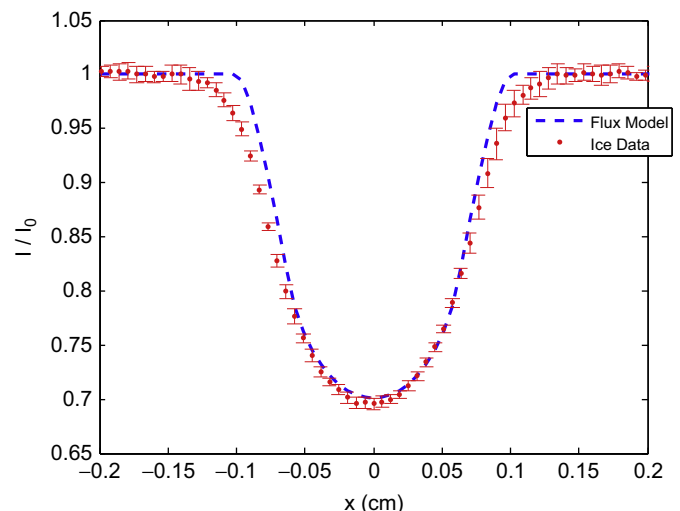

Fig. 9. Measured and predicted neutron attenuation for ice. Ice column profile vs. theoretical expectation from average of eight experiments. R^2 is 0.98.

9. Conclusion

Neutron radiography of a 1.6 mm water column has been performed and density measurements extracted. A ray-tracing model for the neutron flux at the image plane was developed for the University of Texas radiography system that can be easily applied to other imaging systems. This flux model correctly predicts the major features of the radiographs and confirms that a simple attenuation model can be used for density measurements of the geometry used in this study. Density measurements for water and ice were found to be 1.00 ± 0.03 and 0.93 ± 0.03 g/cm^3, respectively, in agreement with published values to within 1% [13]. These results extend current methods and recent results and show that this system can be applied to quantify freezing water in smaller quantities than before.

A limitation of using neutron radiography as opposed to computed tomography for this study is the necessity of assuming a known geometry and a lack of voids in the water. There are applications where these assumptions cannot apply but many engineered systems do constrain the fluid and this method can be utilized for imaging these types of processes. This study focused on the precise measurement of material density. Noise reduction was achieved by averaging data taken over a 180 s time frame. For the study of dynamic systems, this precision can be lessened to gain greater temporal resolution.

To reach higher resolutions, other imaging techniques will be explored. In previous work at the University of Texas TRIGA reactor, a neutron multi-channel plate has been utilized to achieve resolution on the order of 30 μm [12]. Also, a further study of an optimum sample to image plane separation could be explored for this system to maximize the current capabilities. These and other methods will be explored to continue the study of using neutron radiography for high-resolution quantitative phase-change applications.

Acknowledgement

Appendix A. Further explanation of the Matlab flux model

The Matlab script to calculate image plane neutron flux is composed of three nested for-loops:

1. The first loop takes into account the range of angles allowed at the image plane due to a circular primary aperture. That is, the angle of the flux at the image plane will be due to the direct line of sight to the source, in our case a graphite neutron scatterer, through the primary collimator of radius 1 cm. This is shown in Fig. 4 of the main text.
2. The second loop calculates the angle of incidence, from the coordinate, m. As seen in Fig. 4, the maximum angle of incidence would be realized when m is at the full radius of the aperture, which results in an angle of 0.25°. This small angle does have a significant effect on the resulting flux on the image plane, as will be seen in the final result.
3. The third loop calculates the flux at the image plane. The total distance from source to image plane is calculated. At the image plane, the neutron flux will be attenuated by the sample if the
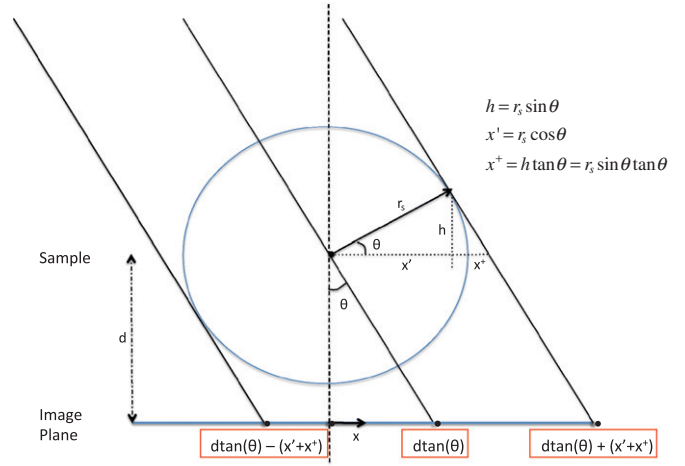

Fig. A.1. Limits of sample attenuation according to image plane coordinates. The sample distance from the image plane is shown as d, θ is the angle of the neutron ray, and r_s is the sample radius. All other variables and geometries are defined in the figure.
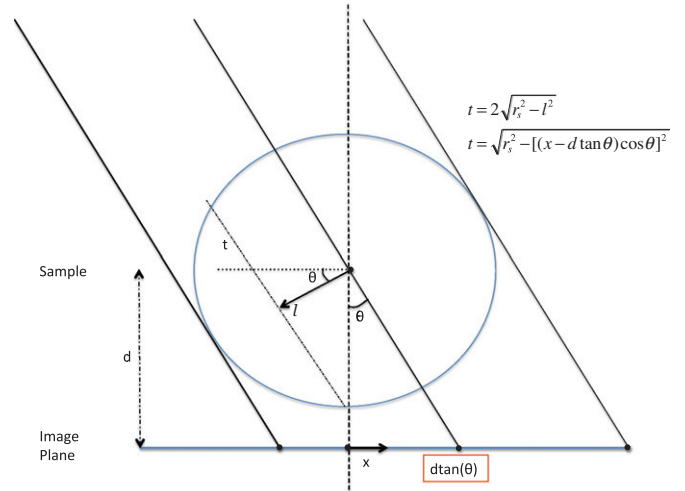
$$h = r_s \sin\theta$$
$$x' = r_s \cos\theta$$
$$x^+ = h\tan\theta = r_s \sin\theta \tan\theta$$

Fig. A.2. Cord length of flux through sample according to image plane coordinates.

$$t = 2\sqrt{r_s^2 - l^2}$$
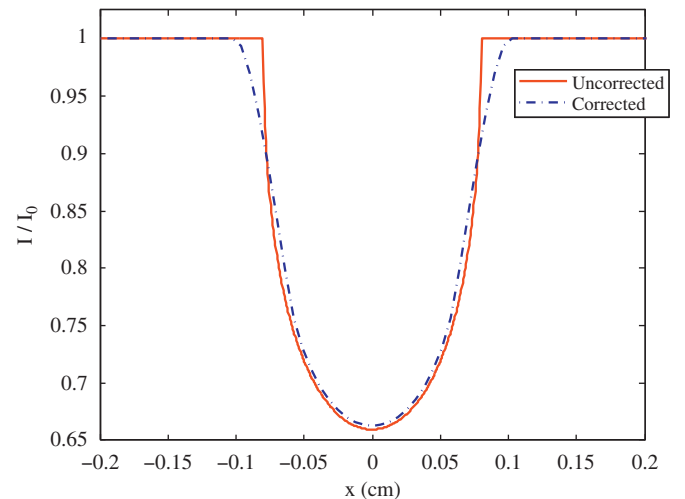$$t = \sqrt{r_s^2 - [(x - d\tan\theta)\cos\theta]^2}$$

Fig. A.3. Matlab simulation resulting image plane flux. Shown are both the corrected flux with angular dependent and the uncorrected plane flux. The biggest effect is noticed at the sample edges ($x \approx \pm 0.1$ cm).

location of flux calculated is located where the incident flux moves through any cord of the sample. Depending on incident angle and location on the image plane, the flux will move through a different cord length of the sample. For the flux moving through the sample, the exponential attenuation is calculated. The equations used to find at what range of image plane coordinates the flux will move through the sample and how much of the sample it will move through are shown in Figs. A.1 and A.2, respectively.

For each incident angle of the flux, the flux across the image plane is calculated according to the above loops and summed with the previous fluxes calculated. The result of this simulation is shown in Fig. A.3. Also plotted for comparison in the figure is the plane flux with a θ of 0.

References

[1] M.R. Deinert, J.Y. Parlange, et al., Journal of Hydrology 290 (2004) 192.
[2] A. Carminati, et al., Advances in Water Resources 30 (2007) 1168.
[3] T. Hibiki, et al., Journal of Nuclear Science and Technology 30 (1993) 516.
[4] L. Pel, et al., International Journal of Heat and Mass Transfer 36 (1993) 1261.
[5] A. Turhan, et al., Journal of Power Sources 160 (2006) 1195.
[6] R.J. Bellows, M.Y. Lin, et al., Journal of the Electrochemical Society 146 (1999) 1099.
[7] A.B. Geiger, A. Tsukada, et al., Fuel Cells 2 (2002) 92.
[8] N. Pekula, K. Heller, et al., Nuclear Instruments and Methods in Physics Research 542 (2005) 134.
[9] A. Turhan, K. Heller, et al., Journal of Power Sources 160 (2006) 1195.
[10] H. Ju, G. Luo, et al., Journal of the Electrochemical Society 154 (2007) B218.
[11] A.K. Heller, et al., Journal of Radioanalytical and Nuclear Chemistry 282 (2009) 183.
[12] L. Cao, Development of a High Spatial Resolution Neutron Imaging System, Ph.D. Thesis, The University of Texas at Austin Austin, TX, May 2007.
[13] 89th edition,David R. Lide (Ed.), CRC Handbook of Chemistry and Physics, vol. 4–6, FL: CRC Press/Taylor and Francis, Boca Raton, 2009.
[14] M. Tamaki, M. Oda, K. Takahashi, W. Tanimoto, T. Funahashi, Nuclear Instruments and Methods in Physics Research A 374 (1996) 345.
[15] M.R. Deinert, et al., IEEE Transactions on Nuclear Science NS52 (2005) 349.
[16] J.R. Lamarsh, A.J. Baratta, Introduction to Nuclear Engineering, Prentice Hall, New Jersey, 2001. (Appendix A).
[17] S. Spern, Initial Characterization of the Cornell Cold Neutron Source, Ph.D. Thesis, Cornell University, Ithaca, NY, January 1998.
[18] G. Knoll, Radiation Detection and Measurement, 3rd ed., John Wiley & Sons, Inc., 2000. (pp. 69, 74, 87–90).